ADVANCED ELECTRONIC MATERIALS
www.advelectronicmat.de

All-Rounder Low-Cost Dopant-Free D-A-D Hole-Transporting Materials for Efficient Indoor and Outdoor Performance of Perovskite Solar Cells

Hong Duc Pham, Sagar M. Jain, Meng Li, Zhao-Kui Wang, Sergei Manzhos, Krishna Feron, Sudhagar Pitchaimuthu, Zhiyong Liu, Nunzio Motta, James R. Durrant, and Prashant Sonar**

A novel biphenyl fumaronitrile as an acceptor and triphenylamine as donor conjugated building blocks are used for the first time to successfully synthesize donor–acceptor–donor molecule (D-A-D) 2,3-bis(4′-(bis(4-methoxyphenyl) amino)-[1,1′-biphenyl]-4-yl)fumaronitrile (TPA-BPFN-TPA). The new TPA-BPFN-TPA with low-lying HOMO is used as a dopant-free hole-transporting material (HTM) in mesoporous perovskite solar cells. The performance of the solar cells using this new HTM is compared with the traditional 2,2′,7,7′-tetrakis(*N*,*N*′-di-p-methoxyphenylamino)- 9,9′-spirobifluorene (Spiro-OMeTAD) HTM based devices for outdoor and indoor performance evaluation. Under 1 sun illumination, dopant-free TPA-BPFN-TPA HTM based devices exhibit a power conversion efficiency (PCE) of 18.4%, which is the record efficiency to date among D-A-D molecular design based dopant-free HTMs. Moreover, the stability of unencapsulated TPA-BPFN-TPA-based devices shows improvement over Spiro-OMeTAD-based devices in harsh relative humidity condition of 70%. Another exciting feature of the newly developed HTM is that the TPA-BPFN-TPA-based devices exhibit improved PCE of 30% and 20.1% at 1000 lux and 200 lux illuminations, respectively. This new finding provides a solution to fabricate low indoor (low light) and outdoor (1 sun) perovskite solar cell devices with high efficiency for cutting-edge energy harvesting technology.

1. Introduction

On account of the global climate change and issues related to energy security, technologies relying on renewable non-fossil energy resources are in demand. Solar energy seems to be one of the best candidates among non-conventional energy resources due to its environmental sustainability and economic viability. To utilize this resource on a large scale, there are a number of developing solar photovoltaic technologies including conventional inorganic solar cells, organic solar cells, dye sensitized solar cells, and perovskite solar cells. Among them, recently perovskite solar cells (PSCs) have emerged as one of the most promising solar cell technologies due to its potentially lower cost and impressive power conversion efficiency (PCE) achieved within a short period of time. Indeed, the PCEs achieved with PSCs grew from 3.8% in 2009 to 25% up to date.[1] Such exceptional development happened due to aggressive

Dr. H. D. Pham, Prof. N. Motta, Prof. P. Sonar
Institute of Future Environment and School of Chemistry, Physics and Mechanical Engineering
Queensland University of Technology (QUT)
2 George Street, Brisbane, Queensland 4001, Australia
E-mail: sonar.prashant@qut.edu.au

Dr. S. M. Jain
Advanced Materials Centre, School of Engineering
London South Bank University
103, Borough Road, London SE10AA, UK
E-mail: sagarmjain@gmail.com

The ORCID identification number(s) for the author(s) of this article can be found under https://doi.org/10.1002/aelm.201900884.

DOI: 10.1002/aelm.201900884

Dr. S. M. Jain, Dr. S. Pitchaimuthu, Prof. J. R. Durrant
College of Engineering
Swansea University Bay Campus
Fabian Way, Swansea SA1 8EN, UK

Dr. M. Li, Prof. Z.-K. Wang
Jiangsu Key Laboratory for Carbon-Based Functional Materials and Devices
Institute of Functional Nano and Soft Materials (FUNSOM)
Soochow University
Suzhou 215123, China

Prof. S. Manzhos
Department of Mechanical Engineering
Faculty of Engineering
National University of Singapore
Block EA #07-08, 9 Engineering Drive 1, Singapore 117576, Singapore

Prof. K. Feron
CSIRO Energy Centre
New South Wales, Newcastle 2304, Australia

Prof. K. Feron
Centre for Organic Electronics
University of Newcastle
Callaghan, New South Wales 2308, Australia

worldwide research efforts. The level of performance achievement in PSC is close to the well-established high-performance solar cell technologies such as copper indium gallium diselenide (CIGS) solar cells and other inorganic materials based solar cells. One of the main reasons for the exceptional efficiency enhancement is due to the outstanding properties of the hybrid organic–inorganic halide perovskite material. These properties include strong solar absorption, large charge carrier diffusion length, and low charge recombination rates.[2,3] Despite achieving the high PCE quickly, stability of the device is one of the major drawbacks holding back commercialization. Fortunately, the development of new materials employed as hole-transporting layers (HTLs) can address this drawback.[4,5] Actually, HTLs play a critical role in PSCs because this layer not only enhances the device performance by blocking electron movement and avoiding charge recombination but also controls the stability of the device by preventing moisture permeation and oxygen penetration into the perovskite layer.[6–9] Development of hole-transporting materials (HTM) is one of the key and growing research topics in perovskite solar cell research domain. Many HTMs have been reported for PSC application. Among them, the HTMs' design based on small molecules and polymers exhibits promising performance. Compared to polymeric counterparts, small molecules possesses several benefits, including high purity, defined molecular structure, promising yield, and better batch-to-batch reproducibility.[8,10] Apart from these newly developed small molecular HTMs, 2,2′,7,7′-tetrakis(*N*,*N*′-dipmethoxyphenylamino)-9,9′-spirbiuorene (Spiro-OMeTAD) has been considered as a standard and most widely used commercial HTM in perovskite solar cells because it dissolves very well in most of the common organic solvents. Such better solubility aspect provides a uniform and smooth surface of the hole-transport layer on top of the active light-absorbing perovskite layer.[9,11] In addition to the above benefit, this material can be also deposited by vacuum-deposition technique, which makes Spiro-OMeTAD as a state-of-the-art HTM for perovskite solar cell technology.[4] Though a significant PCE of 21.1% has been achieved using this standard HTM Spiro-OMeTAD-based devices,[12] there are still some major shortcomings of this material: a) high cost (roughly 400 USD per gram);[10,13] b) multistep synthesis (which leads to the high production cost for commercial solar cells);[3,11] c) the compulsive requirement of additives to enhance the performance of the device (which makes the device unstable in large-area application).[6,14] Apart from these disadvantages of Spiro-OMeTAD, there are almost no reports related to the device performance of PSCs used for indoor applications such as Internet of Things (IoT) with wireless internet connection using this as HTM.[15] Thus, there is urgent demand for a new generation of HTMs that are low cost, scalable, dopant-free, and can provide greater stability to the device with superior performance and their use for indoor application and future smart living.

Dr. Z. Liu
Department of Physics and Materials Science
Henan Key Laboratory of Photovoltaic Materials
Henan Normal University
Xinxiang 453007, China
Prof. J. R. Durrant
Department of Chemistry and Centre for Plastic Electronics
Imperial College London
Exhibition Road, London SW7 2AZ, UK

To avoid charge recombination and prevention of loss of hole-transfer energy, the minimal energy offset between the valence band maximum of perovskite and the highest occupied molecular orbital (HOMO) of hole-transporting layers is needed.[16] This requires a low-lying HOMO level which can be achieved via tuning the HOMO with molecular design approaches. Low-lying HOMO-based HTMs can be designed based on the symmetrical donor–acceptor–donor (D-A-D) design concept, and this class of materials is to satisfy this requirement in comparison to D-π-D, A-D-A, or D-A-π type of molecular structures. First, the symmetrical molecular structures can be beneficial for high hole mobility and improve the lifetime of a charge-separated excited state due to the π–π stacking interaction.[17] Second, the D-A-D structure can provide a deeper HOMO level which leads to the V_{oc} improvement,[18] ultimately to a higher PCE of PSCs.[3,10,19]

Herein, we used an innovative molecular engineering and report a new HTM based on an electron-deficient biphenylfumaronitrile (BPFN) unit as the core and the well-known electron-rich triphenylamine (TPA) as end-capping groups. The compound 2,3-bis(4′-(bis(4-methoxyphenyl)amino)-[1,1′-biphenyl]-4-yl)fumaronitrile designated as TPA-BPFN-TPA is synthesized through a standard Suzuki coupling reaction. The synthesis is illustrated in **Scheme 1**, and the detailed synthesis procedure is explained in Supporting Information. Subsequently, TPA-BPFN-TPA was implemented as HTM in mesoporous $CH_3NH_3PbI_3$ (or $MAPbI_3$) perovskite devices to investigate the effect of this HTL on solar cells' device performance under the condition of outdoor (at 1 sun illumination) and indoor applications (at 1000 lux and 200 lux illumination). Our newly reported D-A-D HTM exhibits excellent performance with efficiency of 30.01% for indoor solar cell device application. While several D-A-D HTMs fabricated in PSCs have been reported,[10,20–24] this is the first report of a novel dopant-free D-A-D-based HTM for indoor application with such impressive efficiency using low-cost materials and device technology.

2. Results and Discussion

2.1. Rational Design and Synthesis

In this molecular structure, the BPFN central core is selected due to its electron-withdrawing nature and its ability to form a low band gap D-A-D type molecular structure upon combining with end-capping donor moiety. In addition to these benefits, BPFN core has been also successfully used for preparing OLED materials with high solid-state efficiency and preparing low band gap organic semiconductors.[25–27] Meanwhile, TPA-substituted conjugated derivatives are often used in high-performance hole-transport materials for several types of solar cells. Particularly, in terms of PSCs, TPA units have proved to be one of the most successful end-capping groups in order to create world class HTMs.[28] BPFN core together with triphenylamine end-capping group conjugated building block has previously been used successfully for constructing materials for organic light emitting diodes (OLEDs) and organic field effect transistor (OFET) devices.[25,26,29] Apart from OLED and OFET applications, BPFN core was not used for PSC devices in previous

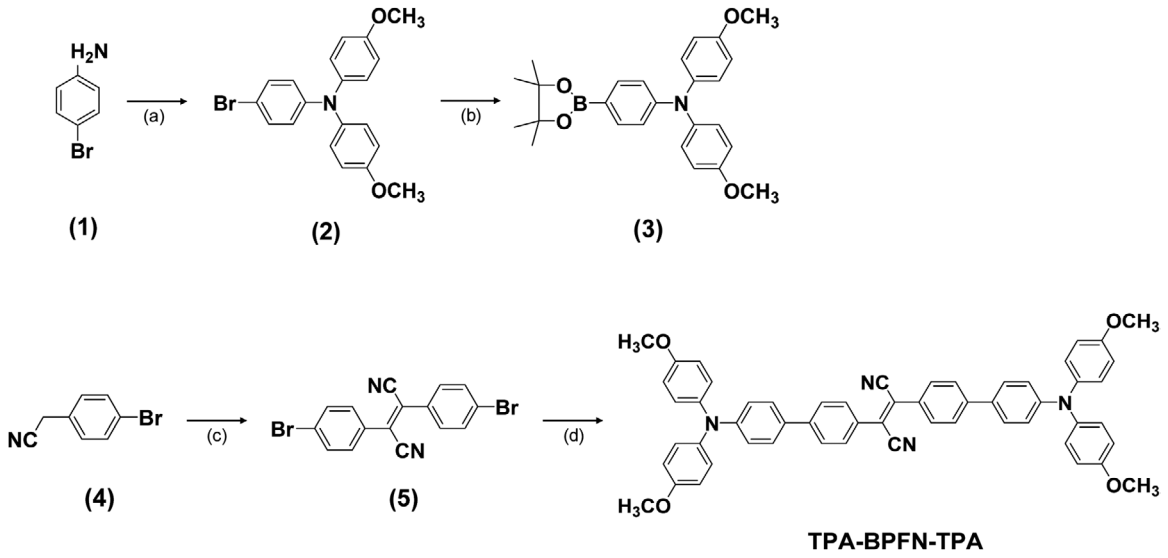

Scheme 1. The synthetic route for TPA-BPFN-TPA. Reagent and conditions: a) 1-iodo-4-methoxybenzene, KOH, CuCl, 1,10-phenanthroline monohydrate, toluene, 120 °C, 24 h; b) bis(pinacolato)diboron, KOAc, $Pd(dppf)Cl_2$, DMF, 120 °C, 24 h; c) 2-(4-bromophenyl)acetonitrile, iodine, sodium methylate, diethyl ether, −78 °C, 4 h; d) 2 M K_2CO_3, toluene, $Pd(PPh_3)_4$, 120 °C,48 h.

reports. Herein, first time, we showed BPFN core can be used successfully for designing a new D-A-D HTM and it can be used successfully for PSC application with a world record for indoor efficiency. The HTMs containing methoxy unit based devices typically show better performance compared to those without these groups under same device characterization conditions, so methoxy group substitution plays a crucial role for highly efficient devices.[30] This is because methoxy units play a Lewis base role to passivate the defect sites at the interface between HTL and the perovskite layer, ultimately leading to increased short circuit current (J_{sc}) and open circuit voltage (V_{oc}).[31] Furthermore, the methoxy moieties enhance the solubility of the molecules for easy processability.[9]

The synthesis route of TPA-BPFN-TPA is represented in Scheme 1. The preparation of precursor TPA (compound **3**) followed previous studies.[3,8] The synthesis of BPFN core was performed from the commercial available 2-(4-bromophenyl) acetonitrile (compound **4**) and followed earlier attempts.[25,26] Afterward, the synthesis of target TPA-BPFN-TPA was carried out via a Suzuki coupling reaction between compounds (**3**) and (**5**) using tetrakistriphenylphosphine palladium [$Pd(PPh_3)_4$] catalyst and 2 M K_2CO_3 base at 120 °C for 48 h in anhydrous toluene solvent. After purification by SiO_2 column, the reaction yield for the compound was measured around 60%. Their purity was proved by proton and C13 nuclear magnetic resonance (NMR) spectroscopy (Figure S1, Supporting Information). Meanwhile, the molecular weight was confirmed by mass spectroscopy. TPA-BPFN-TPA is well soluble in most common organic solvents such as chloroform, dichloromethane, and chlorobenzene.

2.2. Density Functional Theory Calculations

To gain insight about the distribution of electron density and the energy levels of this material, density functional theory (DFT) calculations at the B3LYP level using the basis set Lanl2dz were conducted.[32] A polarized continuum model of the chloroform solvent was used.[33] The resulting HOMO and LUMO distributions are shown in **Figure 1**. The electronic structure of the LUMO primarily dispersed over the π-conjugated system through the electron withdrawing BPFN core, whereas the HOMO is mainly delocalized over the electron-donating TPA moieties and two central weak donor phenyl rings and the olefin bond. This observation coincides well with earlier attempts, which have the similar structural design.[25,26] The computed LUMO and HOMO values are −3.03 and −5.01 eV, respectively. Accordingly, the band gap is found to be of 1.98 eV, in good agreement with experimental data. The absolute HOMO and LUMO values are somewhat higher that the experimental estimates, due to approximations used in both the calculation (functional, basis set) and the experiment (PESA uncertainly and LUMO estimate from onset of absorption). In addition to above data, the DFT shows the optical absorption maximum in chloroform is at 737 nm, resulting in a narrow optical band gap of 1.68 eV. Thus, peak is due to the HOMO-to-LUMO transition. It is red-shifted versus the experimental peak (in the 500 nm area as shown in **Figure 2**a) due to the charge-transfer nature of the transition, as expected. The low band gap of the TPA-BPFN-TPA is due to the insertion of donor–acceptor building blocks in the backbone and their molecular orbital interactions. On the other hand, the computed Stokes shift is 32 nm, in good agreement with experimental 30 nm (counted from the VIS peak at 499 nm in solution). The dihedral angle between end-capping TPA groups and the adjacent phenyl moiety of BPFN core is computed to be 32°.

2.3. Optical Properties

The optical properties of TPA-BPFN-TPA were measured by UV–vis spectroscopy. The normalized absorption spectra in

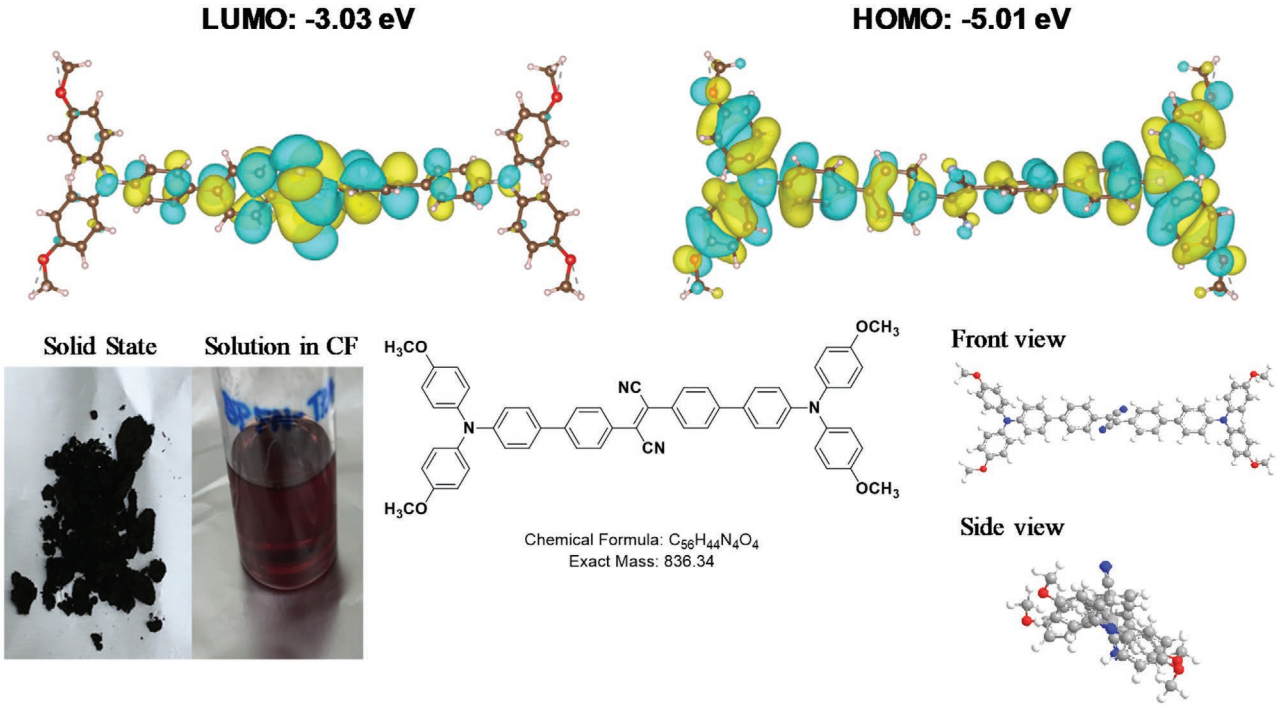

Figure 1. The calculated isosurfaces of electron density of HOMO and LUMO and the geometry of TPA-BPFN-TPA.

chloroform (CF) solutions and solid-state thin films on glass are illustrated in Figure 2a. The extracted optical parameters are listed in **Table 1**. The similarity of the spectra of the material in the thin films and solutions suggests that there is no significant crystallization in thin films.[13] The absorption maxima of TPA-BPFN-TPA reveals two main absorption peaks, which is consistent with the data from DFT calculation shown in Figure S3, Supporting Information. The UV peak in the 300–370 nm

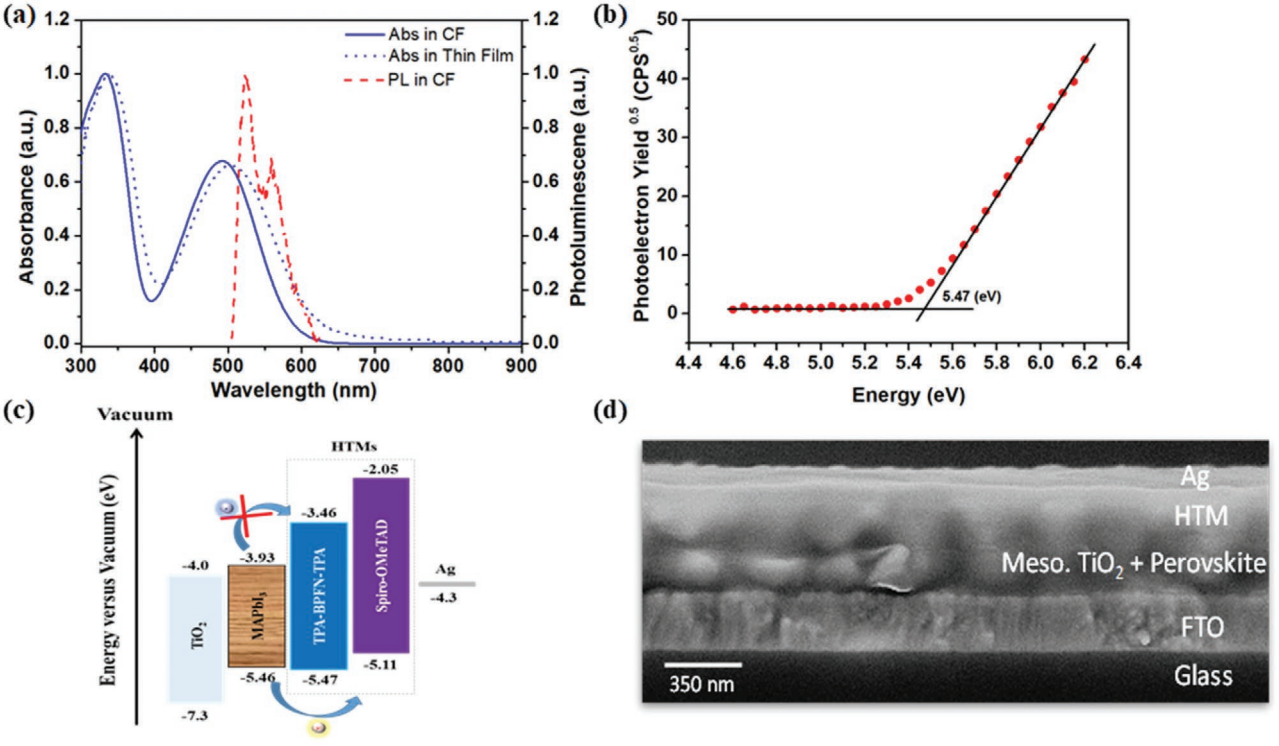

Figure 2. a) The UV–vis absorption and PL spectra in CF solutions and the UV–vis absorption in films; b) photoelectron spectroscopy in air (PESA) spectra; c) energy level diagram, d) cross-sectional scanning electron microscopy image of PSC of TPA-BPFN-TPA.

Table 1. Thermal, optical, and electrochemical properties of TPA-BPFN-TPA.

HTM	λ_{max} [nm]		λ_{PL} [nm]	Stoke shift [nm]	E_g^{opt} [c] [eV]	E_{HOMO} [d] [eV]	E_{LUMO} [d] [eV]	T_d [°C]	T_g [°C]	T_m [°C]	μ [$cm^2 V^{-1} s^{-1}$]
	Solution[a]	Film[b]									
TPA-BPFN-TPA	492	499	522	30	2.01	−5.47	−3.46	390	110	240	2.9×10^{-4}

[a]Absorption spectrum was measured in chloroform (CF) solution; [b]Film was prepared by spin-coating a CF solution containing the sample onto glass substrate at a spin speed of 1000 rpm at room temperature; [c]Optical bandgap was calculated from the formula of $1240/\lambda_{onset}$; [d]The oxidation potential was also measured by photoelectron spectroscopy in air (PESA); ELUMOPESA = EHOMOPESA + E_g^{opt}.

area is due to n–π^* transitions of TPA units.[34] The visible peak in the 400–600 nm area is due to the HOMO-to-LUMO transition and involves partial charge transfer (CT) between the donor and acceptor moieties of the D-A molecules.[26] The absorption band in films is slightly red-shifted compared with that of the solutions, which indicates very weak intermolecular interactions in the solid state.[10]The absorption maxima in chloroform solutions shows two peaks at 332 and 492 nm, and that in thin films exhibit at 337 and 499 nm. Moreover, the optical band gap from the onset of absorption curve in solid state is evaluated to be 2.01 eV.

The normalized emission maxima in chloroform solutions of the TPA-BPFN-TPA is shown in Figure 2a and listed in Table 1. The first strong peak at 522 nm and a fairly shifted shoulder peak at 559 nm may be tentatively attributed to the n–π^* transition and intramolecular charge transfer (ICT) transition, respectively.[35] To understand the relationship between the absorption and emission, the Stoke shift is calculated by using the gap between the maximum of absorption and emission spectra. As a result, the value is found to be roughly 30 nm, which indicates a relatively rigid nature of the TPA-BPFN-TPA structure.

2.4. Thermal Properties

The thermal properties of TPA-BPFN-TPA were characterized by using thermogravimetric analysis (TGA) and differential scanning calorimetry (DSC), which are shown in Figure S2, Supporting Information, and summarized in Table 1. For TGA plot, the temperature at which 5% weight loss is observed is 390 °C, indicating that the thermal stability is sufficient for the fabrication as well as operation of PSCs, including at high ambient temperatures. The DSC curve with two cycles shows that the glass transition and melting temperatures are found to be at 110 and 240 °C, respectively. While the presence of methoxy groups in TPA units of TPA-BPFN-TPA in this study does not affect the glass transition temperature, methoxy groups were the reason causing a noticeable change in the decomposition temperature (as shown in Table S1, Supporting Information).[25,26]

2.5. Electrochemical Properties

The electronic structure of molecules plays an important role for charge injection and transport and the simplest method to determine its energy level is to find out its HOMO and LUMO values. These values are also crucial for demonstrating environmental stability of the new material. HOMO energy level of TPA-BPFN-TPA was estimated by using photoelectron spectroscopy in air (PESA). The corresponding data is shown in Table 1. From the onset energy level using PESA data, we calculated HOMO value for TPA-BPFN-TPA HTM and the HOMO value in thin film is estimated to be −5.47 eV. The PESA data are shown in Figure 2b. This value implies good energy band alignment with the HOMO of active light-absorbing perovskite material. As argued above, such a small HOMO value offset between the perovskite active layer and the HTM can facilitate the hole extraction and transport by reduced charge recombination and loss of energy transfer. Compared to other D-A-D HTMs employed in mesoporous PSCs, which are summarized in Table 4, the design of TPA-BPFN-TPA achieved the goal of the low-lying HOMO level.

Meanwhile, the LUMO value was estimated from the difference between the HOMO estimated by PESA and optical band gap calculated from thin film optical absorption data using ELUMO = EHOMO + E_g^{opt} equation. The obtained LUMO value is −3.46 eV which is sufficiently high and sufficient to block the electron movement which can further enhance solar cell efficiency. Based on the HOMO-LUMO value, TPA-BPFN-TPA seems to be potential promising material for the hole-transporting layer of perovskite solar cells.

2.6. Perovskite Solar Cells

Upon completion of new HTM characterization, TPA-BPFN-TPA was employed in the conventional mesoporous perovskite devices with the purpose to study the impact of the presence of the hole-transporting layer on the device performance. PSC devices with the same architecture (FTO/compact-TiO_2/mesoporous-TiO_2/$MAPbI_3$/HTL/Ag) were prepared as in an earlier report.[36] The energy level of each layer in the device is depicted in Figure 2c. Meanwhile, the scanning electron microscope cross-section of the mesoscopic device is shown in Figure 2d. A dense compact TiO_2 layer (30–40 nm) was deposited on the FTO substrate by spray pyrolysis while a mesoporous n-type TiO_2 layer was formed by spin-coating dilute TiO_2 paste. The $MAPbI_3$ was then spin-coated by solvent engineering reported by Seok´s group.[37]

The perovskite solution was prepared by dissolving 50 wt% of $MAPbI_3$ in the mixed dimethyl sulfoxide (DMSO) and γ-butyrolactone (GBL) DMSO/GBL. Around 120 nm thick HTLs were applied to the top $MAPbI_3$ layer by spin-coating. Finally,

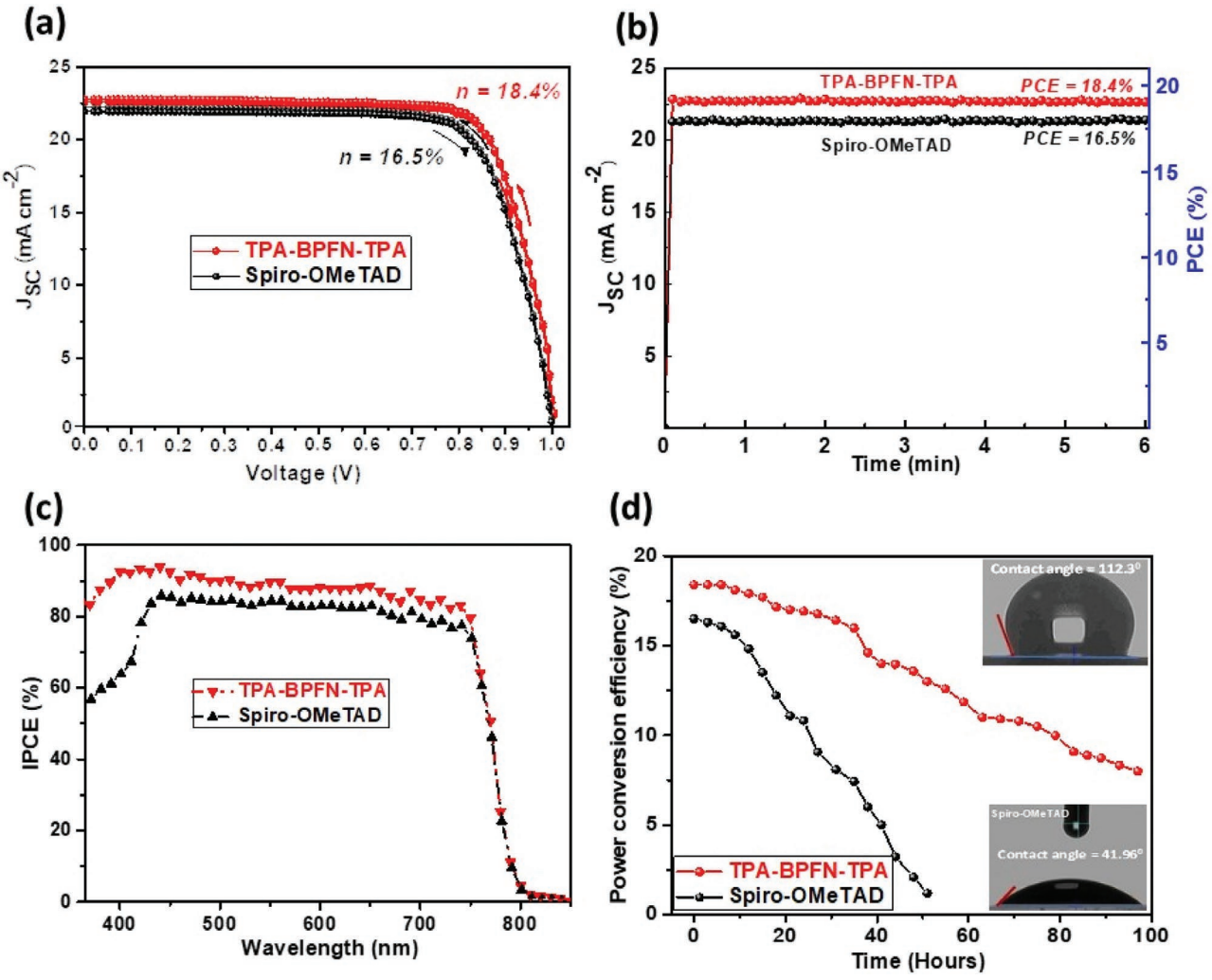

Figure 3. Photovoltaic performance with hysteresis of optimized champion PSC devices made using different hole-transport layers: a) using TPA-BPFN-TPA (red curve) and Spiro-OMeTAD (black curve) as the hole-transporting material; b) absolute EQE spectra of PSC devices made using hole-transporting layers; c) power output under maximum power point tracking for 360 s, starting from forward bias and resulting in a stabilized power output of 18.4% and 16.5% using TPA-BPFN-TPA and Spiro-OMeTAD based devices, respectively. All devices were measured at constant low scan speed of 10 mV s^{-1}; d) stability measurements at maximum power point for unencapsulated devices prepared using TPA-BPFN-TPA and Spiro-OMeTAD hole-transporting layers. All devices were kept in relative humidity 70% and under continuous 1 sun (AM 1.5 G) illumination PCE obtained on maximum power point tracking. Inset images show contact angle measurements performed on FTO/perovskite/respective HTMs assembly.

silver as a counter electrode was deposited by thermal evaporation. The thickness of mesoporous TiO_2 and perovskite is ≈550 nm, whereas the capping layer of perovskite is estimated to be ≈100 nm. Bigger crystals of TiO_2 in the capping layer assist in saturated light absorption enhancing the external quantum efficiency (EQE) in the red-light range. For a valid comparison of performance in terms of PCE and stability, we prepared new dopant-free (undoped) HTM based devices and standard devices with dopant using conventional Spiro-OMeTAD (with additional additives, including *t*BP and LiTFSI) as the HTM. The optimized champion device efficiency for three different HTMs and corresponding photovoltaic performance parameters are shown in **Figure 3**a,b and **Table 2**. The TPA-BPFN-TPA HTM based PSC device shows the highest champion device efficiency of 18.4% with respect to a J_{sc} of 22.70 mA cm^{-2}, a V_{oc} of 1.04 V, and an *FF* of 78% while an overall PCE of 16.5% is recorded with a J_{sc} of 22.3 mA cm^{-2}, a V_{oc} of 1.0 V, and an *FF* of 74% in case of doped Spiro-OMeTAD-based devices. Moreover, devices prepared with pristine TPA-BPFN-TPA and doped Spiro-OMeTAD exhibited negligible hysteresis.

Interestingly, as shown in **Figure 4** and **Table 3**, the low light performance of undoped TPA-BPFN-TPA-based solar cells also shows significant improvement of 30.01% and 20.1% over doped Spiro-OMeTAD PSCs' 22.7% and 10% at 1000 lux and 200 lux illumination, respectively.

It is noteworthy that the obtained PCE of 18.4% (at 1 sun) and 30.01% (at 1000 lux) using TPA-BPFN-TPA HTM is a record compared to other HTMs reported in the literature taking the dopant-free aspect into account.[38] Even though the first report regarding inverted perovskite solar cells using PEDOT:PSS as HTM was carried out by Prof. Lin's research group,[39] there is no attempt utilizing dopant-free HTMs

Table 2. Solar cell device performance with different HTMs under 1 sun condition.

HTLs[a)]	Scan direction	V_{oc} [V]	J_{sc} [mA cm^{-2}]	*FF* [%]	PCE [%]
Undoped TPA-BPFN-TPA	Forward	1.04	22.70	78.0	18.40
	Reverse	1.02	22.63	76.1	17.54
	Average[b)]	0.93	21.22	76.1	15.06
Doped Spiro-OMeTAD[c)]	Forward	1.00	22.31	74.0	16.50
	Reverse	1.00	21.97	71.5	16.60
	Average[b)]	0. 86	20.00	74.3	12.01

[a)]Cell size (active area): 0.100 cm^2. Photovoltaic performance at 1000 wm^{-2} (AM 1.5 G) and constant scan speed of 10 mV s^{-1} mesoscopic $MAPbI_3$ devices; [b)]An average device efficiency of a total of 43 devices for each Spiro-OMeTAD and TPA-BPFN-TPA, respectively; [c)]With additives: 4-*tert*-butylpyridine (*t*BP) and Li-bis(trifluoromethanesulfonyl)-imide (LiTFSI).

fabricated in mesoporous $MAPbI_3$ PSCs up to date. In this study, we have demonstrated for the first time the effect of changing dopant-free D-A-D HTM/mesoporous perovskite interface on the performance of PSCs under low light illumination for indoor application or application of mesoporous solar cells in low insolation regions or weather conditions. The statistics of a total of 86 devices (43 devices using each HTMs) prepared using three different hole-transporting layers is given in Figure S4, Supporting Information. The statistical data exhibit an average device efficiency of 15% and 12%, respectively, showing improved reproducibility in indoor (under 200 lux and 1000 lux illuminations) as well as outdoor (under 1 sun illumination) performance for PSCs made using TPA-BPFN-TPA over Spiro-OMeTAD-based devices. As presented in Figure 3c, the devices with TPA-BPFN-TPA have EQE values above 85% from 365 to 650 nm covering the entire UV region with the highest EQE of 94% observed at 420 nm.

The hole-transport properties are measured using the space charge limited current (SCLC) method. A simple device architecture with configuration of ITO/PEDOT-PSS/HTM/Au were made to measure the hole-only mobility of respective hole transport materials. The ITO and gold have a close matching work function value of 5.3 eV that acts as a hole-only device and makes it possible to determine the hole mobility. The calculated hole mobility value of TPA-BPFN-TPA is 2.90×10^{-4} V^{-1}s^{-1}, whereas that of Spiro-OMeTAD shows relatively low 1.45×10^{-4} V^{-1}s^{-1} (Figure S5, Supporting Information). Our newly developed low-cost D-A-D type dopant-free HTM almost exhibits two times higher hole mobility than the conventional expensive Spiro-OMeTAD with dopant and this is also one of the remarkable features of our new material. Higher hole mobility obtained for TPA-BPFN-TPA compared to Spiro-OMeTAD are further confirmed from the high *FF* obtained for devices prepared using TPA-BPFN-TPA HTMs.

Water solubility of Pb makes lead-based PSCs highly susceptible for degradation and is also a major environmental concern,[40] especially when the ambience is humid. This raises the question of the stability of these solar cells. In our previous study we have investigated a notorious role played by LiTFSI salt dopants in the degradation of PSCs.[13] We investigated the stability of fabricated champion devices without any encapsulation at high humidity conditions (relative humidity [RH] = 70%, temperature = 22 °C) for our newly developed TPA-BPFN-TPA and standard classical Spiro-OMeTAD HTMs based PSCs (as shown in Figure 3d). Stability measurements were performed using a simple stability setup as previously reported.[13] The doping of hygroscopic salts (LiTFSI) induces more hydrophilic nature of cells prepared using doped Spiro-OMeTAD. The performances of TPA-BPFN-TPA and Spiro-OMeTAD on aging are detailed in Figure 3d. The stability measurements show that the doped Spiro-OMeTAD HTM based devices degraded at a faster rate compared to undoped TPA-BPFN-TPA HTM based devices.

As expected, it is found that the undoped TPA-BPFN-TPA is more stable than the doped Spiro-OMeTAD. The hydrophilic nature of the Spiro-OMeTAD, which is due to doping with LiTFSI hygroscopic salt,[13] is further confirmed by the

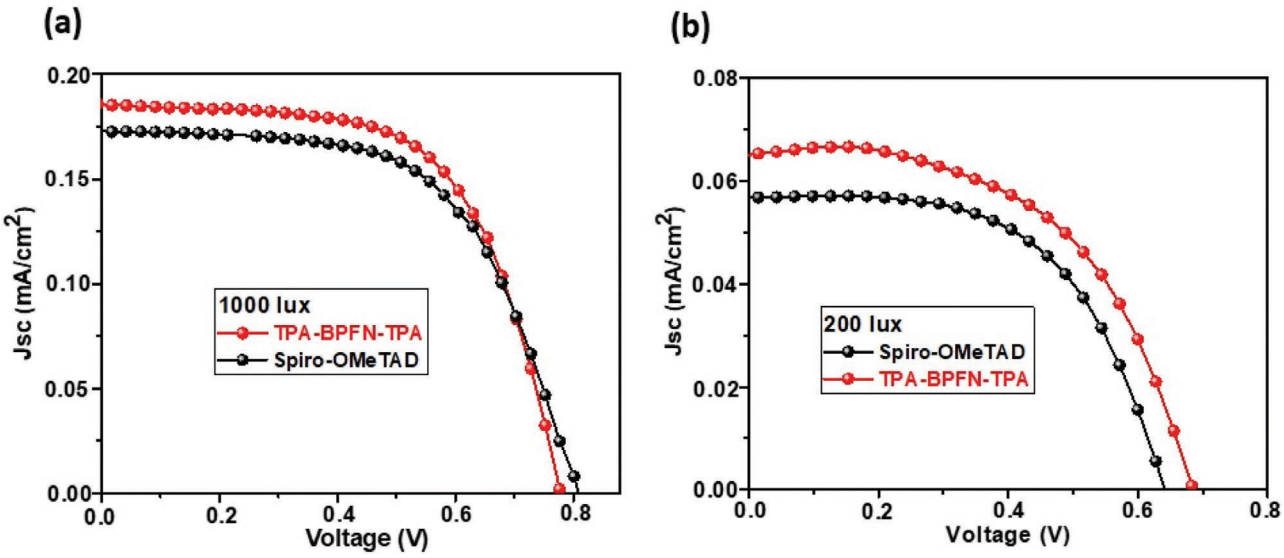

Figure 4. Photovoltaic performance of perovskite devices prepared using TPA-BPFN-TPA and Spiro-OMeTAD HTMs under 1000 lux (a) and 200 lux (b) illumination.

Table 3. Champion (Champ) and average (Ave) performance of PSCs fabricated employing **TPA-BPFN-TPA** and Spiro-OMeTAD HTMs under indoor light illumination (1000 lux and 200 lux).

Illumination	HTL	V_{oc} [V]	J_{sc} [mA cm^{-2}]	*FF* [%]	PCE [%]
1000 lux	Doped Spiro-OMeTAD (Champ.)	0.809	0.171	65	22.70
	Doped Spiro-OMeTAD (Ave)	0.600	0.130	50	15.50
	Undoped TPA-BPFN-TPA (Champ.)	0.796	0.186	74	30.01
	Undoped TPA-BPFN-TPA (Ave.)	0.700	0.176	69	24.50
200 lux	Doped Spiro-OMeTAD (Champ.)	0.645	0.058	41	10.31
	Doped Spiro-OMeTAD (Ave.)	0.502	0.038	29	6.03
	Undoped TPA-BPFN-TPA (Champ.)	0.698	0.066	59	20.14
	Undoped TPA-BPFN-TPA (Ave.)	0.610	0.062	56	17.43

water contact angle measurements performed on the glass/perovskite/Spiro-OMeTAD surface, where a low contact angle of 41° is observed, indicating high wettability. On contrary, the glass/perovskite/TPA-BPFN-TPA surface displays a high contact angle of 112° (shown in the inset of Figure 3d), which is three times higher indicating the water-repellent nature of the dopant-free TPA-BPFN-TPA surface. This also ultimately contributes to the improved stability of devices prepared using undoped TPA-BPFN-TPA HTL.

On exposing the champion devices to RH = 70%, we observed a rapid decrease in the PCE of Spiro-OMeTAD-based PSCs causing rapid loss in efficiency from 16.5% to 5% after only 40 h. The devices made using TPA-BPFN-TPA showed an improved stability and over 100 h of exposure to intense 70% RH showed a drop in PCE from 18.4% to 8%. The improved performance and stability of TPA-BPFN-TPA over Spiro-OMeTAD is due to the high hole-transport properties and avoidance of hygroscopic dopants (e.g., LiTFSI).

To further investigate the origin of the improved PCE of 18.4% obtained with TPA-BPFN-TPA, steady-state and time-resolved photoluminescence measurements are carried out and shown in **Figure 5**. In order to avoid quenching contribution from TiO_2, all measurements are performed on a glass/perovskite/HTM assembly. In this way, we ensure that any changes in PL are due to the HTM. The glass/perovskite film was used as a reference. All films were excited at 550 nm wavelength. The steady-state PL (as shown in Figure 5a) of the glass/perovskite exhibits high-intensity photoluminescence (black spectrum) confirming the excellent quality of perovskite films that we used in this study.[36,41] Upon the deposition of Spiro-OMeTAD and TPA-BPFN-TPA HTMs, the PL intensity reduces, showing significant quenching of 70% and 93%, respectively. We have observed a similar behavior in our earlier studies.[10,13] The higher photoluminescence quenching with TPA-BPFN-TPA clearly indicates more efficient charge transfer and is well matched with the high hole mobility obtained for TPA-BPFN-TPA.

Time-resolved photoluminescence shown in Figure 5b indicates the improved hole-transport properties. Bare perovskite films deposited on glass substrate as well as with different hole-transport layers show the usual biphasic kinetics. The fast component decays in picosecond (due to 80 ps laser pulse) and the slower component has a time constant of 10–15 ns. The fast component represents trap filling. As the hole transfer films are deposited on the bare glass–perovskite layer for direct probing, this gives us a good estimation about quenching of the photoluminescence happening only due to hole-transport layers. As shown in our previous work, a good quality glass–perovskite sample shows a lifetime of 8–10 ns.[41] In this work, we have obtained ≈8 ns lifetime for the bare perovskite sample (without

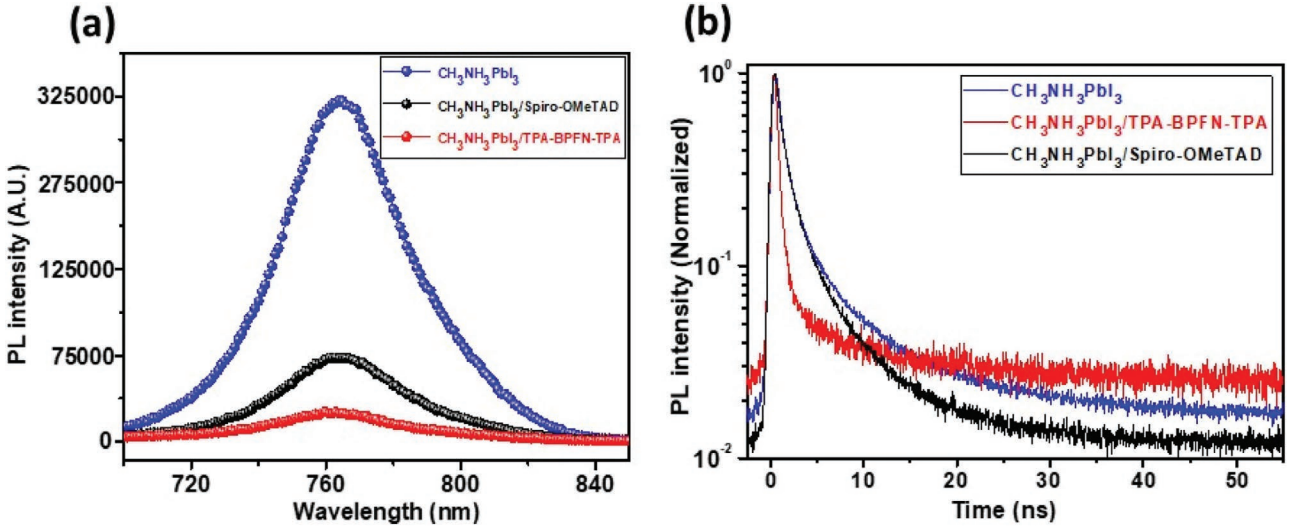

Figure 5. a) Steady state and b) time-resolved photoluminescence (PL) measured on bare perovskite film (black), and hole-transport layers TPA-BPFN-TPA and Spiro-OMeTAD deposited on perovskite.

Table 4. The comparison among promising D-A-D HTMs.

HTM[a)]	HOMO [eV]	LUMO [eV]	E_g^{opt} [eV]	Perovskite materials (Energy levels)[b)]	Active area [cm^2]	Additives[c)]	V_{oc} [V]	J_{sc} [mA cm^{-2}]	*FF* [%]	PCE [%]	Stability test [%][d)]	Ref.
TPA-BPFN-TPA	−5.47	−3.46	2.01	$MAPbI_3$ (−5.46/−3.93 eV)	0.1	None	1.04	22.7	78	18.4 (16.6)[e)]	76 (5)[f)]	This study
DPA-ANT-DPA	−5.46	−4.03	1.43	$MAPbI_3$ (−5.46/−3.93 eV)	0.1	None	1.00	16.2	71	11.5 (16.0)	66 (14)	[10]
YN2	−5.40	−3.57	1.83	$(FAPbI_3)_{0.85}(MAPbBr_3)_{0.15}$ (−5.65/−4.05 eV)	0.126	LiTFSI *t*BP	1.11	23.15	75	19.27 (17.8)	91.3 (42.2)	[23]
TQ2	−5.32	−2.94	2.38	$MAPbI_3$ (−5.44/−3.93 eV)	0.09	LiTFSI *t*BP	1.12	22.55	77.67	19.62 (18.54)	90 (60)	[24]
BTPA-3	−5.42	−3.13	2.29	$Cs_{0.05}(MA_{0.17}FA_{0.83})_{0.95}Pb(I_{0.83}Br_{0.17})_3$ (−5.4 eV)	0.16	LiTFSI *t*BP	1.09	19.9	53.4	9.81 (13.2)	84 (98)	[22]
				$MAPbBr_3$ (−5.90/−3.60 eV)			1.44	6.66	61.5	5.91 (5.61)	75 (91)	
H1	−5.46	−2.62	2.92	$MAPbBr_3$	0.16	LiTFSI *t*BP FK209	1.43	5.50	72	5.80 (6.12)	—	[21]

[a)]A typical mesoporous architecture, including FTO/compact TiO_2/mesoporous TiO_2/Perovskite/HTM/cathode, was used in these studies; [b)]Energy levels of perovskite materials (HOMO/LUMO [eV]); [c)]bis(trifluoromethylsulfonyl)imide lithium salt (LiTFSI), 4-*tert*-butylpyridine (*t*BP), tris(2-(1*H*-pyrazol-1-yl)-4-*tert*-butylpyridine)cobalt(III) tri[hexafluorophosphate] (FK209); [d)]The percentage of the retaining performance after the ageing test (unsealed devices); [e)]PCE of standard Spiro-OMeTAD; [f)]The percentage of the retaining performance of standard Spiro-OMeTAD.

the hole-transporting layer), which is similar to the earlier attempts. In the company of the high intensity PL, this further confirms the quality of the perovskite film. Bare perovskite film shows an average life time of 200 ns. After the introduction of TPA-BPFN-TPA as the material of the hole-transporting layer above the perovskite layer, the average decay time (τ) shortened to ≈20.2 ns. The decay lifetime (τ_1) of Spiro-OMeTAD and TPA-BPFN-TPA hole-transporting materials decreased from 35 ns (bare perovskite without HTL) to 15 ns for Spiro-OMeTAD and 9 ns for TPA-BPFN-TPA HTL.

A list of small molecular D-A-D-type HTMs recently reported is summarized in **Table 4**. These selected HTMs are based on a similar mesoporous architecture with approximately equivalent working area. Generally, most HTMs are doped to improve the device performance. Aside from them, The highest PCE of 19.62% is achieved with the devices using dopant-free TQ2 HTM. However, the presence of additives has a negative impact on the stability of the devices and increases the production cost. Along with doped D-A-D HTMs, the champion efficiency of our TPA-BPFN-TPA-based devices is 18.4% in the absence of additives. Moreover, the J_{sc} of 22.7 mA cm^{-2} and *FF* of 78% of devices using TPA-BPFN-TPA HTM are among the best values in dopant-free D-A-D HTM employed in these conventional mesoporous PSCs. More interestingly, the HOMO energy levels of TPA-BPFN-TPA, DPA-ANT-DPA, and H1 are close to that of perovskite layer compared to other D-A-D HTMs. Particularly, despite the similar HOMO energy levels (5.46–5.47 eV), their PCE-based devices are in the order: TPA-BPFN-TPA > DPA-ANT-DPA > H1. This corresponds to the different J_{sc} values (TPA-BPFN-TPA > DPA-ANT-DPA > H1). In terms of aging tests of unsealed devices, the devices using novel TPA-BPFN-TPA as HTM exhibit an outstanding stability compared to the reference Spiro-OMeTAD devices under similar condition. Furthermore, the devices with TPA-BPFN-TPA HTL have been employed for indoor applications (low light) while this application of other HTMs was not reported. According to the tabular comparison, our newly reported small molecular HTM shows a superior PCE compared to other recent HTMs. Thus, TPA-BPFN-TPA can become a worthy alternative to Spiro-OMeTAD.

3. Conclusions

In this work, we have successfully designed and synthesized a new BPFN core based TPA-BPFN-TPA hole-transport material which is employed without the addition of hygroscopic additives (e.g., LiTFSI) in a mesoporous perovskite architecture yielding a record efficiency of 18.4%, which is higher than that of doped standard Spiro-OMeTAD under 1 sun condition. Particularly, in terms of indoor applications, our undoped TPA-BPFN-TPA-based devices displayed significant, hysteresis-free efficiency of 30% and 20.1% at 1000 lux and 200 lux illumination, respectively. To the best of our knowledge, these are record efficiencies to date for dopant-free TPA-based hole-transport material in mesoporous $MAPbI_3$ devices for outdoor and indoor applications. Most importantly, TPA-BPFN-TPA-based devices revealed improved stability over Spiro-OMeTAD-based devices under similar aging condition without encapsulation. Overall, the superior performance and stability of TPA-BPFN-TPA- to Spiro-OMeTAD-based devices is due to the high hole-transport characteristics as observed from hole mobility, well efficient photoluminescence quenching, and hydrophobic nature, respectively. Based on our outstanding resultant data, the symmetrical geometric D-A-D design will become a promising architecture for dopant-free HTMs of highly efficient and more stable solution-processable perovskite solar cells in the future. This work paves a plethora of HTMs to be used to fine tune PSCs performance for harvesting indoor light efficiently and hence extend their application for Internet of Things (IOTs).

4. Experimental Section

Detailed experimental methods can be found in Supporting Information.

Supporting Information

Supporting Information is available from the Wiley Online Library or from the author.

Acknowledgements

H.D.P. and S.M.J. contributed equally to this work. H.D.P. is thankful to QUT for offering the QUTPRA scholarship to conduct his research work. Some of the data reported in this paper were obtained at the Central Analytical Research Facility operated by the Institute for Future Environments (QUT). Access to CARF is supported by generous funding from the Science and Engineering Faculty (QUT). S.M.J. is thankful to the Welsh assembly Government funded Sêr Cymru Solar project, the EPSRC grants EP/M025020/1 (Supergen Solar Challenge), and the Marie-Curie COFUND fellowship for financial support. S.M. is supported by the Ministry of Education of Singapore. Additionally, this project has received funding from the European Union's Horizon 2020 research and innovation programme under the Marie Skłodowska-Curie grant agreement No. 663830 and the UKRI Global Challenge Research Fund project SUNRISE (EP/P032591/1). P.S. is thankful to QUT for the financial support and to the Australian Research Council for the Future Fellowship grant FT130101337. N.M. acknowledges the support of the Queensland Government via the Q-CAS funding scheme.

Conflict of Interest

The authors declare no conflict of interest.

Keywords

biphenyl fumaronitrile, dopant-free materials, perovskite solar cells, triphenylamine

Received: August 18, 2019
Revised: December 6, 2019
Published online:

[1] a) NREL, Best reesearch-cell efficiencies, http://www.nrel.gov/ncpv/images/efficiency_chart.jpg (accessed: December 2019); b) A. Kojima, K. Teshima, Y. Shirai, T. Miyasaka, *J. Am. Chem. Soc.* **2009**, *131*, 6050.
[2] M. A. Green, A. Ho-Baillie, H. J. Snaith, *Nat. Photonics* **2014**, *8*, 506.
[3] H. D. Pham, Z. Wu, L. K. Ono, S. Manzhos, K. Feron, N. Motta, Y. Qi, P. Sonar, *Adv. Electron. Mater.* **2017**, *3*, 1700139.
[4] Z. Hawash, L. K. Ono, Y. Qi, *Adv. Mater. Interfaces* **2018**, *5*, 1700623.
[5] W. Zhou, Z. Wen, P. Gao, *Adv. Energy Mater.* **2018**, *8*, 1702512.
[6] N. H. Tiep, Z. Ku, H. J. Fan, *Adv. Energy Mater.* **2016**, *6*, 1501420.
[7] X. Liu, Y. Wang, E. Rezaee, Q. Chen, Y. Feng, X. Sun, L. Dong, Q. Hu, C. Li, Z.-X. Xu, *Sol. RRL* **2018**, *2*, 1800050.
[8] H. D. Pham, H. Hu, K. Feron, S. Manzhos, H. Wang, Y. M. Lam, P. Sonar, *Sol. RRL* **2017**, *1*, 1700105.
[9] X. Zhao, M. Wang, *Mater. Today Energy* **2018**, *7*, 208.
[10] H. D. Pham, K. Hayasake, J. Kim, T. T. Do, H. Matsui, S. Manzhos, K. Feron, S. Tokito, T. Watson, W. C. Tsoi, N. Motta, J. R. Durrant, S. M. Jain, P. Sonar, *J. Mater. Chem. C* **2018**, *6*, 3699.
[11] B. Xu, J. Zhang, Y. Hua, P. Liu, L. Wang, C. Ruan, Y. Li, G. Boschloo, E. M. J. Johansson, L. Kloo, A. Hagfeldt, A. K. Y. Jen, L. Sun, *Chem* **2017**, *2*, 676.
[12] M. Saliba, T. Matsui, J.-Y. Seo, K. Domanski, J.-P. Correa-Baena, M. K. Nazeeruddin, S. M. Zakeeruddin, W. Tress, A. Abate, A. Hagfeldt, M. Grätzel, *Energy Environ. Sci.* **2016**, *9*, 1989.
[13] H. D. Pham, T. T. Do, J. Kim, C. Charbonneau, S. Manzhos, K. Feron, W. C. Tsoi, J. R. Durrant, S. M. Jain, P. Sonar, *Adv. Energy Mater.* **2018**, *8*, 1703007.
[14] H. J. Snaith, M. Grätzel, *Appl. Phys. Lett.* **2006**, *89*, 262114.
[15] a) H. K. H. Lee, J. Wu, J. Barbé, S. M. Jain, S. Wood, E. M. Speller, Z. Li, F. A. Castro, J. R. Durrant, W. C. Tsoi, *J. Mater. Chem. A* **2018**, *6*, 5618; b) M. Li, C. Zhao, Z.-K. Wang, C.-C. Zhang, H. K. H. Lee, A. Pockett, J. Barbé, W. C. Tsoi, Y.-G. Yang, M. J. Carnie, X.-Y. Gao, W.-X. Yang, J. R. Durrant, L.-S. Liao, S. M. Jain, *Adv. Energy Mater.* **2018**, *8*, 1801509.
[16] a) L. K. Ono, Y. Qi, *J. Phys. Chem. Lett.* **2016**, *7*, 4764; b) Q.-D. Ou, C. Li, Q.-K. Wang, Y.-Q. Li, J.-X. Tang, *Adv. Mater. Interfaces* **2017**, *4*, 1600694.
[17] M. Cheng, B. Xu, C. Chen, X. Yang, F. Zhang, Q. Tan, Y. Hua, L. Kloo, L. Sun, *Adv. Energy Mater.* **2015**, *5*, 1401720.
[18] J. M. Jiang, P. A. Yang, H. C. Chen, K. H. Wei, *Chem. Commun.* **2011**, *47*, 8877.
[19] a) K. Liu, Y. Yao, J. Wang, L. Zhu, M. Sun, B. Ren, L. Xie, Y. Luo, Q. Meng, X. Zhan, *Mater. Chem. Front.* **2017**, *1*, 100; b) P. Ganesan, K. Fu, P. Gao, I. Raabe, K. Schenk, R. Scopelliti, J. Luo, L. H. Wong, M. Grätzel, M. K. Nazeeruddin, *Energy Environ. Sci.* **2015**, *8*, 1986; c) S. Park, J. H. Heo, C. H. Cheon, H. Kim, S. H. Im, H. J. Son, *J. Mater. Chem. A* **2015**, *3*, 24215; d) K. Do, H. Choi, K. Lim, H. Jo, J. W. Cho, M. K. Nazeeruddin, J. Ko, *Chem. Commun.* **2014**, *50*, 10971.
[20] a) F. Wu, Y. Ji, C. Zhong, Y. Liu, L. Tan, L. Zhu, *Chem. Commun.* **2017**, *53*, 8719; b) Y. C. Chen, S. K. Huang, S. S. Li, Y. Y. Tsai, C. P. Chen, C. W. Chen, Y. J. Chang, *ChemSusChem* **2018**, *11*, 3225.
[21] S. Carli, J. P. Baena, G. Marianetti, N. Marchetti, M. Lessi, A. Abate, S. Caramori, M. Gratzel, F. Bellina, C. A. Bignozzi, A. Hagfeldt, *ChemSusChem* **2016**, *9*, 657.
[22] G. Wu, Y. Zhang, R. Kaneko, Y. Kojima, Q. Shen, A. Islam, K. Sugawa, J. Otsuki, *J. Phys. Chem. C* **2017**, *121*, 17617.
[23] P. Xu, P. Liu, Y. Li, B. Xu, L. Kloo, L. Sun, Y. Hua, *ACS Appl. Mater. Interfaces* **2018**, *10*, 19697.
[24] H. Zhang, Y. Wu, W. Zhang, E. Li, C. Shen, H. Jiang, H. Tian, W.-H. Zhu, *Chem. Sci.* **2018**, *9*, 5919.
[25] X. Han, Q. Bai, L. Yao, H. Liu, Y. Gao, J. Li, L. Liu, Y. Liu, X. Li, P. Lu, B. Yang, *Adv. Funct. Mater.* **2015**, *25*, 7521.
[26] Y. Ma, X. Cao, G. Li, Y. Wen, Y. Yang, J. Wang, S. Du, L. Yang, H. Gao, Y. Song, *Adv. Funct. Mater.* **2010**, *20*, 803.
[27] a) H.-C. Yeh, S.-J. Yeh, C.-T. Chen, *Chem. Commun.* **2003**, 2632; b) Y. T. Lee, C. L. Chiang, C. T. Chen, *Chem. Commun.* **2008**, 217.
[28] a) J. Wang, K. Liu, L. Ma, X. Zhan, *Chem. Rev.* **2016**, *116*, 14675; b) P. Agarwala, D. Kabra, *J. Mater. Chem. A* **2017**, *5*, 1348; c) H. D. Pham, L. Xianqiang, W. Li, S. Manzhos, A. K. K. Kyaw, P. Sonar, *Energy Environ. Sci.* **2019**, *12*, 1177.
[29] S. Kim, S. J. Yoon, S. Y. Park, *J. Am. Chem. Soc.* **2012**, *134*, 12091.
[30] a) X. Sun, Q. Xue, Z. Zhu, Q. Xiao, K. Jiang, H.-L. Yip, H. Yan, Z. A. Li, *Chem. Sci.* **2018**, *9*, 2698; b) A. Magomedov, S. Paek, P. Gratia, E. Kasparavicius, M. Daskeviciene, E. Kamarauskas, A. Gruodis, V. Jankauskas, K. Kantminiene, K. T. Cho, K. Rakstys, T. Malinauskas, V. Getautis, M. K. Nazeeruddin, *Adv. Funct. Mater.* **2018**, *28*, 1704351; c) F. Cai, J. Cai, L. Yang, W. Li, R. S. Gurney, H. Yi, A. Iraqi, D. Liu, T. Wang, *Nano Energy* **2018**, *45*, 28.
[31] S. J. Park, S. Jeon, I. K. Lee, J. Zhang, H. Jeong, J.-Y. Park, J. Bang, T. K. Ahn, H.-W. Shin, B.-G. Kim, H. J. Park, *J. Mater. Chem. A* **2017**, *5*, 13220.
[32] a) A. D. Becke, *J. Chem. Phys.* **1993**, *98*, 5648; b) P. Hohenberg, W. Kohn, *Phys. Rev.* **1964**, *136*, B864; c) W. Kohn, L. Sham, *Phys. Rev.* **1965**, *140*, A1133.
[33] J. Tomasi, B. Mennucci, R. Cammi, *Chem. Rev.* **2005**, *105*, 2999.

[34] X. Liu, L. Zhu, F. Zhang, J. You, Y. Xiao, D. Li, S. Wang, Q. Meng, X. Li, *Energy Technol.* **2017**, *5*, 312.
[35] W. Liu, Z. Chen, C.-J. Zheng, X.-K. Liu, K. Wang, F. Li, Y.-P. Dong, X.-M. Ou, X.-H. Zhang, *J. Mater. Chem. C* **2015**, *3*, 8817.
[36] S. M. Jain, B. Philippe, E. M. J. Johansson, B.-W. Park, H. Rensmo, T. Edvinsson, G. Boschloo, *J. Mater. Chem. A* **2016**, *4*, 2630.
[37] N. J. Jeon, J. H. Noh, Y. C. Kim, W. S. Yang, S. Ryu, S. I. Seok, *Nat. Mater.* **2014**, *13*, 897.
[38] a) S. Kazim, F. J. Ramos, P. Gao, M. K. Nazeeruddin, M. Grätzel, S. Ahmad, *Energy Environ. Sci.* **2015**, *8*, 1816; b) J. Liu, Y. Wu, C. Qin, X. Yang, T. Yasuda, A. Islam, K. Zhang, W. Peng, W. Chen, L. Han, *Energy Environ. Sci.* **2014**, *7*, 2963; c) M. Franckevičius, A. Mishra, F. Kreuzer, J. Luo, S. M. Zakeeruddin, M. Grätzel, *Mater. Horiz.* **2015**, *2*, 613; d) Y.-K. Wang, Z.-C. Yuan, G.-Z. Shi, Y.-X. Li, Q. Li, F. Hui, B.-Q. Sun, Z.-Q. Jiang, L.-S. Liao, *Adv. Funct. Mater.* **2016**, *26*, 1375.
[39] C.-Y. Chen, J.-H. Chang, K.-M. Chiang, H.-L. Lin, S.-Y. Hsiao, H.-W. Lin, *Adv. Funct. Mater.* **2015**, *25*, 7064.
[40] A. Babayigit, D. Duy Thanh, A. Ethirajan, J. Manca, M. Muller, H. G. Boyen, B. Conings, *Sci. Rep.* **2016**, *6*, 18721.
[41] S. M. Jain, Z. Qiu, L. Häggman, M. Mirmohades, M. B. Johansson, T. Edvinsson, G. Boschloo, *Energy Environ. Sci.* **2016**, *9*, 3770.